

IMECE2018-87817

**TOWARDS DEVELOPMENT OF SOLAR DISTRICT HEATING SYSTEM IN
KAZAKHSTAN: A CASE STUDY – AN ANALYSIS OF HYBRID THERMAL ENERGY
STORAGE PERFORMANCE**

Bakytzhan Akhmetov
Al-Farabi Kazakh National
University
Almaty, Kazakhstan

Tangnur Amanzholov
GreenWell Mechanics
Almaty, Kazakhstan

Abzal Seitov
Al-Farabi Kazakh National
University
Almaty, Kazakhstan

Bakytnur Berdenova
Al-Farabi Kazakh National
University
Almaty, Kazakhstan

Amankeldy Toleukhanov
Satbayev University
Almaty, Kazakhstan

Madina Tungatarova
Satbayev University
Almaty, Kazakhstan

Assetzhan Koldas
Al-Farabi Kazakh National
University
Almaty, Kazakhstan

ABSTRACT

There are number of thermal energy-intensive appliances installed in buildings. They are heating, ventilation, air conditioning and hot water systems, which account for substantial fraction of total building energy consumption. One of the effective ways to decrease the amount energy consumption of these appliances from traditional grids, is to utilize renewable energy sources, especially solar energy, as the main thermal energy supplier. However, because of unpredictable nature of solar radiation, it is difficult to supply necessary amount of thermal energy to aforementioned appliances without the assistance of effective storage. Thermal storage system helps to balance instantaneous differences between demand and supply of thermal energy using off-peak excess energy, which might be lost otherwise. Therefore, development of a storage that can store thermal energy harvested from renewable energy sources has high importance and one of the active research areas among scientists.

In order to efficiently store solar energy, it is possible to combine two perspective heat storages as a kind of a hybrid system - latent heat accumulator for short-term storage (STS) and borehole thermal energy storage (BTES) for seasonal storage. The authors of the current study have been funded by

World Bank for 2017-19 to construct aforementioned hybrid system in Almaty, Kazakhstan. In the current research paper, they will provide their experimental and numerical research results related to the integration of BTES and STS studies for the heating application of buildings.

INTRODUCTION

A number of different technologies that make possible the use of solar energy for space heating (SH) and domestic hot water (DHW) supply is being suggested by different authors [1]. The main problem with using the solar energy for these purposes, is its daily and seasonal variations and inconstancy. Therefore, in order to deliver thermal energy continuously for the SH and DHW systems, the solar energy must be stored for further utilization. Storage of solar energy in huge amounts allows its use all year round, regardless the time and weather conditions [2].

Different medium like water, phase change materials (PCM) and ground are being considered as energy storing medium. For example, Thermal Energy Storage Tank (TEST) and Aquifer Thermal Energy Storage (ATES) constitute a seasonal solar thermal energy storage systems (SSTES) where the water is a storing medium. Each of them have their advantages and

disadvantages. In the case of TEST, there is a high probability of water leakage problems [3]. Whereas in the case of ATES (i) the chemicals composition of the groundwater may cause corrosion of the metal equipment and piping system when circulating through the system; (ii) the groundwater flow may wash away the stored thermal energy and (iii) possible problems with clogging of hot/cold water wells, since the soil or rock usually easily enters the open circuit of the ATES circulation and so on.

When using ground as storing medium the average density of thermal energy is 60-70 kJ/kg. Main advantage of geothermal accumulator is its scalability as any number of new borehole heat exchangers can be added to the main boreholes system. Therefore, there is no volume limitation even if the energy density is low. As the circulation of the water occurs in a closed loop, therefore there is no direct interaction of soil and groundwater with the water circulating in the system.

The phase change materials have high storage density which is a huge advantage, which is about 330 kJ/kg, but they are expensive and have negative characteristics like volume change, phase segregation and low thermal conductivity that limits its wide distribution [3],[4]. New composite PCM materials with improved thermal conductivity and capacity are being developed in order to increase the systems efficiency and performance [5-19].

In the present paper the performance of Hybrid Thermal Energy Storage system analyzed for different scenarios:

- (i) Solar thermal energy collected by the means of solar collectors directly goes to the STS accumulator that constitutes a vessel/tank filled with water and PCM containers which are placed in three concentric circles within the tank. The experimental investigation of thermo-physical properties of pure and nano- Al_2O_3 added paraffin waxes (PW) in the current study were carried out applying appropriate methods and facilities. Mathematical model which considers phase change, heat and mass transfer, the processes that occur during the systems operation of the STS, was developed. The systems performance was predicted via numerical simulation using *Comsol Multiphysics Software* for given materials.
- (ii) On the place of the BTES construction the TRT test was carried out. It allows to define whether the soil/rock of the terrain is suitable for heat storage, and give essential information about location's geological formation and geophysical properties. It is undesirable to have an aquifer layers because the groundwater flows depending on the current velocity can cause energy loss. The BTES performance for cases of active and inactive aquifers, or in other words, for two different current velocities namely 0, 10 cm/day where investigated numerically using Finite Difference Method. The depth of the borehole heat exchangers is taken to be 30 m, and from 12 to 18 m it is assumed to have a confined aquifer layer.
- (iii) Optimization of well pattern is of a key importance while constructing BTES accumulator. The set of borehole heat

exchangers (BHE) has a cylindrical form. In summer when the solar radiation is abundant, the excess thermal energy goes for charging the geothermal accumulator. The heat carrier passes the group of BHE from the center to the edge of the cylinder, and vice versa while discharging. The performance of the BTES varies depending on the distance between borehole heat exchangers and the well pattern. The present paper shows temperature distribution in the geothermal accumulator for the cases of active and inactive aquifers.

I. SHORT TERM STORAGE

1.1 Concept of sequentially connected latent heat storages

Figure 1 illustrates the concept of sequentially connected TES filled with pure or Al_2O_3 -added PWs each having various phase change temperatures (PCT). When the solar heated working fluid is available to be stored for later applications, it is pumped into TES 1, where heat is transferred to the PCM with the high PCT. The remaining thermal energy is further sequentially delivered to TES 2 where the PCM has low PCT. Thus, the working fluid gradually cools as it leaves TES 2 and returns to the solar collectors to further operate in the closed loop. Once the PCMs in both TESs is fully melted the charging process stops. In case of the discharging mode, the flow direction is reversed, where working fluid first enters the LHS 2 with PCM having low PCT, and then LHSs filled with PCM having high PCT, thus gradually gaining thermal energy from the sequentially connected TES to deliver the energy for heating application purposes.

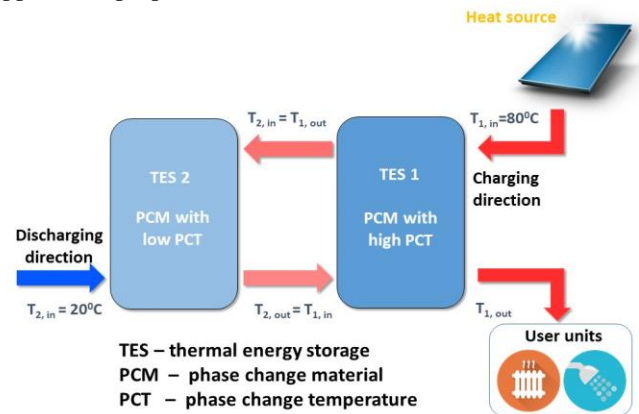


Figure 1. Schematic illustration of the sequentially connected TES system

Detailed illustration of the TES and its design features are shown in **Figure 2**. The storage vessel with 1.05 m height and 0.74 m diameter has 27 containers filled with PCM. PCM containers have circular cross section with diameter 0.09 m and height 95 cm. 27 PCM containers are placed as three concentric circles: external circle contains 16 of them, while the middle and inner circles have 8 and 3 containers respectively as shown in **Figure 2**. The storage vessel and PCM containers are made of AISI type 316 stainless steel. There are inlet apertures at the

bottom of each PCM container to evenly deliver the working fluid into the storage tank. Similarly, outlet apertures are also located on the top of each PCM containers. Such distribution of inlet and outlet apertures improves the charging and discharging rate of each PCM containers, as if they are functioning as stand-alone TES. In the numerical studies, depending on the charging/discharging direction, the temperature and velocity of outlet apertures of the neighboring TES (**Figure**) are used as the inlet conditions for inlet apertures of next TES in the sequence.

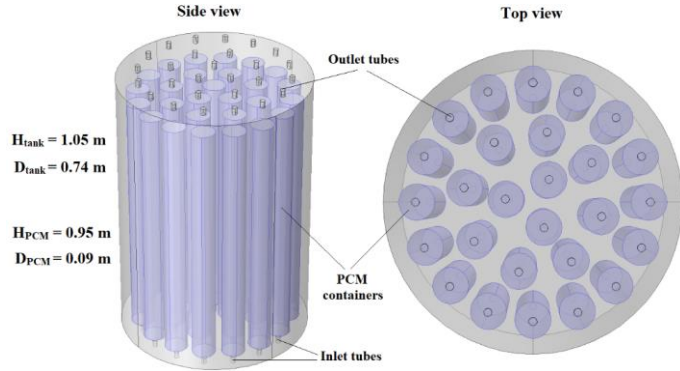


Figure 2. Design of the TES

1.2 Mathematical modeling

The simulation of the processes within the LHSs is based on a three-dimensional (3D) space and time-dependent numerical analysis using Comsol Multiphysics. In fact, 3D simulation provides complete velocity field of the working fluid, solid-liquid interaction in terms of the pressure field, and thermal field within both PCM containers and the TES. Therefore, the dimensions of the computational domain coincide with the actual LHS design illustrated in **Figure 2**. In order to avoid unnecessary numerical calculations, some physical processes that have minor impact on the physics of the processes in the LHS were not taken into account. Thus, in the present numerical studies, the following assumptions were made:

1. Heat transfer does not occur between LHS and its surroundings since the vessel is insulated from all sides;
2. Fluid flow within the TES is considered as laminar;
3. Heat transfer through the PCM is conductive without free convection effect. In fact, the PCM is heated from all its sides though the walls of the slim circular container, hence, it takes little time to achieve completely melted PCM. In addition, paraffin is quite viscous when melted, therefore, it assumed that free convection does not significantly affect the heat transfer process between PCM and the working fluid;
4. In case of the PCM containers filled with Al_2O_3 -PCMs, they are considered as homogeneous composite materials, and discontinuities in terms of the heat transfer across the highly conductive aluminum nanoparticles are negligible since amount of the nanoparticles constitute 2% and 4% of the PCM weight. Consequently, for transient thermal analysis by the numerical simulation, the effective thermal properties of the

Al_2O_3 -PCMs are applied measured by the characterization techniques described above.

In the numerical calculations, the mass and momentum equations (1.1) and (1.2) for incompressible fluid were used to describe the flow of the working fluid in the TES and the resulting velocity field is used in energy equation (1.3) to calculate the thermal field in the TES [20-21]:

$$\frac{\partial u}{\partial x} + \frac{\partial v}{\partial y} + \frac{\partial w}{\partial z} = 0 \quad (1.1)$$

$$\left. \begin{aligned} \rho_f \frac{\partial u}{\partial t} + \rho_f \left(\frac{\partial(uu)}{\partial x} + \frac{\partial(uv)}{\partial y} + \frac{\partial(uw)}{\partial z} \right) &= \\ -\nabla p_f + \mu_f \left(\frac{\partial^2 u}{\partial x^2} + \frac{\partial^2 u}{\partial y^2} + \frac{\partial^2 u}{\partial z^2} \right) & \\ \rho_f \frac{\partial v}{\partial t} + \rho_f \left(\frac{\partial(vu)}{\partial x} + \frac{\partial(vv)}{\partial y} + \frac{\partial(vw)}{\partial z} \right) &= \\ -\nabla p_f + \mu_f \left(\frac{\partial^2 v}{\partial x^2} + \frac{\partial^2 v}{\partial y^2} + \frac{\partial^2 v}{\partial z^2} \right) & \end{aligned} \right\} \quad (2)$$

$$\left. \begin{aligned} \rho_f \frac{\partial w}{\partial t} + \rho_f \left(\frac{\partial(wu)}{\partial x} + \frac{\partial(wv)}{\partial y} + \frac{\partial(ww)}{\partial z} \right) &= \\ -\nabla p_f + \mu_f \left(\frac{\partial^2 w}{\partial x^2} + \frac{\partial^2 w}{\partial y^2} + \frac{\partial^2 w}{\partial z^2} \right) + F_z & \\ \rho_f c_f \frac{\partial T}{\partial t} + \rho_f c_f \left(u \frac{\partial T_f}{\partial x} + v \frac{\partial T_f}{\partial y} + w \frac{\partial T_f}{\partial z} \right) &= \end{aligned} \right\} \quad (1.3)$$

$$\left(\frac{\partial}{\partial x} (k_f \frac{\partial T}{\partial x}) + \frac{\partial}{\partial y} (k_f \frac{\partial T}{\partial y}) + \frac{\partial}{\partial z} (k_f \frac{\partial T}{\partial z}) \right) + Q$$

Phase change processes in the PCM containers were modelled using the apparent heat capacity method coupled with the energy equation. According to the apparent heat capacity method, the latent heat is included in the heat capacity of the PCM as an additional term, and it is suitable to include solid-solid, solid-liquid liquid-solid phase transitions in desired order. Thus, the energy equation is:

$$\left. \begin{aligned} \rho_p c_p \frac{\partial T}{\partial t} + \rho_p c_p \left(u \frac{\partial T}{\partial x} + v \frac{\partial T}{\partial y} + w \frac{\partial T}{\partial z} \right) &= \\ \left(\frac{\partial}{\partial x} (k_p \frac{\partial T}{\partial x}) + \frac{\partial}{\partial y} (k_p \frac{\partial T}{\partial y}) + \frac{\partial}{\partial z} (k_p \frac{\partial T}{\partial z}) \right) + Q & \end{aligned} \right\} \quad (1.4)$$

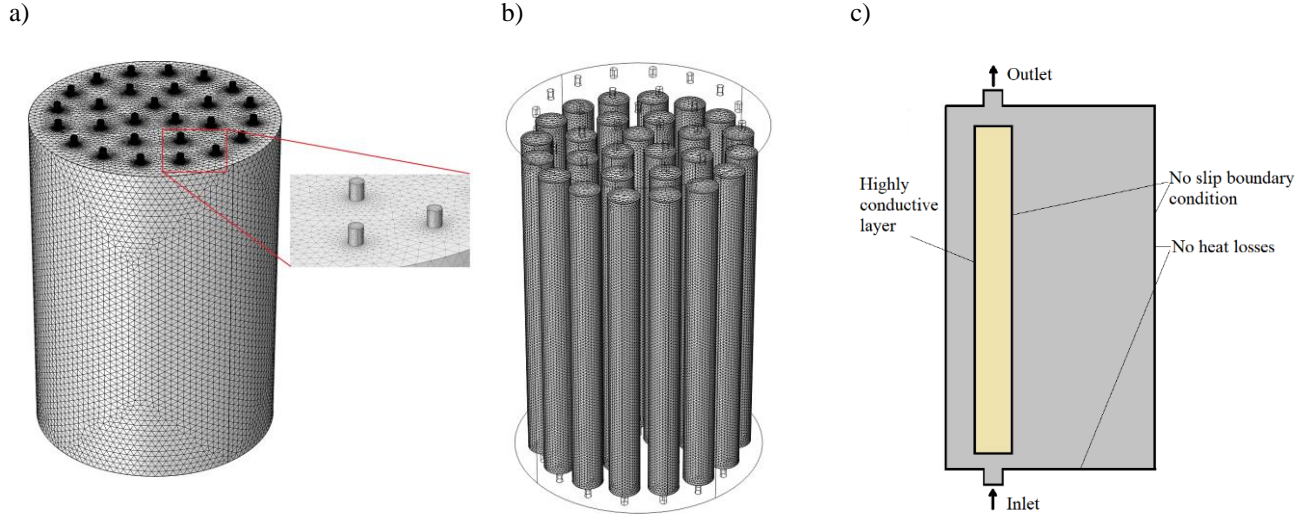


Figure 3. a) Meshing of the TES; b) Meshing of the PCM containers; c) Schematic description of the boundary conditions

Density, heat capacity and thermal conductivity equations that takes into account the phase change processes [22-23]:

$$\rho_{PCM} = \theta\rho_{phase1} + (1 - \theta)\rho_{phase2} \quad (1.5)$$

$$c_{p,PCM} = \frac{1}{\rho}(\theta\rho_{phase1}c_{p,phase1} + (1 - \theta)\rho_{phase2}c_{p,phase2}) + L\frac{d\alpha}{dT} \quad (1.6)$$

$$k = \theta k_{phase1} + \theta k_{phase2} \quad (1.7)$$

$$\alpha = \frac{1 - \theta}{2} \frac{\rho_{phase2} - \theta\rho_{phase1}}{\theta\rho_{phase1} + (1 - \theta)\rho_{phase2}} \quad (1.8)$$

Moreover, it is assumed that the phase transition occurs in a temperature interval $T_{PC} - \Delta T/2$ and $T_{PC} + \Delta T/2$, where ΔT is the difference between the temperatures of phase change start and completion. In ideal case, $1 - \theta$ operate as the Heaviside function, that is, equal to 0 before phase change temperature T_{PC} and 1 after T_{PC} and $\frac{d\alpha}{dT}$ function as the Dirac pulse.

Therefore, last term in the equation (1.6) is the enthalpy jump at phase change temperature $\frac{d\alpha}{dT}$ that is added in the form of

latent heat. Moreover, since convective flow is not taken into account in the PCM containers, convective term in the energy equation (1.4) is not considered. Heat source term Q is neglected both in (1.3) and (1.4) due to the absence of heat source in the storage tank and PCM containers.

The fluid flow domain takes place within the TES while the phase change processes takes place in the PCM containers. Therefore, equations (1.1) and (1.2) are solved at the nodes of the mesh that occupies the fluid flow domain in the TES as shown in Figure 3, a) and the resulting velocity field is coupled with equation (1.3) to obtain the thermal field in the same numerical domain. Figure 3, b) shows the meshing of the numerical domain related to the PCM containers, where equations (1.4)-(1.7) were solved numerically by taking into account the heat transfer processes between the working fluid and the PCMs. With the purpose of justifying the validity of the numerical results a grid dependence test was performed on the temperature variation of PCM as a function of charging time. Pure paraffin wax (PW1) was considered as PCM and its temperature change was averaged across the containers to analyze the grid dependence of the numerical results regarding the phase transition of PCM in the storage tank.

Mass conservation and energy balance were analysed using the post-processing tools for calculating integrated quantities for each solution in a data set. Thus, by selecting the boundaries or volumes on which the integral should be carried out, the mass conservation equation can be written as [22]:

$$\int_V \frac{\partial \rho_f}{\partial t} dV + \int_S \rho_f U \cdot n dS = 0 \quad (1.9)$$

Due to the incompressibility of the working fluid which is water in the current studies, the first term in the equation is related to the volume integral of the mass conservation in the storage tank is negligible. The second term can be written to the surface integral of the mass flow at the inlet and outlet apertures, the sum of which must be zero:

$$\int_{S,inlet} \rho_f U \cdot n dS_{inlet} + \int_{S,outlet} \rho_f U \cdot n dS_{outlet} = 0 \quad (1.10)$$

Table 1. Thermo-physical properties of pure and nano-Al₂O₃ added paraffin waxes (PW1 and PW2).

	Latent heat of melting and peak		Latent heat of cooling and peak		Average thermal diffusivity enhancement (in percentage)		Average specific heat capacity (kJ/kg K)		Average density (kg/m ³)	
	kJ/kg	°C	kJ/kg	°C	Solid state	Liquid state	Solid state	Liquid state	Solid state	Liquid state
PW1	158.14	48.31	158.52	41.12	-	-	2.12	1.68	816.8	770.9
PW1 +Al ₂ O ₃ (2%)	↓152.98	↓47.08	↓153.07	↓41.03	↑ 20 %	↑ 29 %	↓2.02	↓1.6	↓807.1	↓761.9
PW1 +Al ₂ O ₃ (4%)	↓148.33	↓46.92	↓148.23	↓40.64	↑ 41 %	↑ 39 %	↓1.9	↓1.45	↓800.6	↓755.7
PW2	183.15	66.29	183.16	59.78	-	-	1.94	1.89	834.1	791.5
PW2 +Al ₂ O ₃ (2%)	↓180.97	↓65.77	↓180.08	↓59.30	↑ 11 %	↑ 15 %	↓1.84	↓1.72	↓823.4	↓784
PW2 +Al ₂ O ₃ (4%)	↓178.69	↓65.64	↓178.44	↓59.10	↑ 22 %	↑ 25 %	↓1.66	↓1.56	↓815.2	↓774.8

At each time step during the numerical simulation, the relative mass difference between the inlet and outlet was checked and it was equal to approximately 10^{-5} which was less than the relative tolerance value for the solver set to 0.001.

1.3 Initial and boundary conditions

Initially, the temperatures of all TES including their parts were at 20°C, while the velocity of the working fluid within the fluid flow domains was initially zero in both cases. No-slip boundary condition was applied to the fluid flow at the solid surfaces. The heat losses from the sides of the TES to the environment were assumed to be negligible while the metal PCM containers were approximated as highly conductive layers without thermal resistance. Temperature at the inlet pipes of the TES having the highest PCT during the charging case was maintained at 80 °C and the inlet temperatures of the consequent LHSs were taken to be equal to the outlet from the preceding TES since they are sequentially connected to each other. During the discharging case the inlet temperature of the TES with the lowest PCT is set to 20 °C and the inlet temperatures of the subsequent TES are considered as equal to the outlet temperatures of the preceding TES in the sequence as shown in **Figure 1**. The inlet velocities are altered in order to find the efficient charging and discharging velocity.

1.4 Characterization of thermal properties

Understanding the heat transfer processes and the variation of the thermal properties of PCMs in relation to the solid-liquid and liquid-solid phase transitions throughout the temperature range of interest is the prerequisite to develop energy efficient technologies based on PCMs. Several PCMs, including

paraffin, have relatively low thermal diffusivity and thermal conductivity, which hinders them to be widely used in thermal systems. The development of PCMs enhanced with nanomaterials is one of the promising solutions to improve their low thermal properties. Addition of nanomaterials might lead to property changes, such as, shifting of the phase transition temperature range, variation of the density and the energy storage capacity of the PCM [5-18]. Therefore, studying of the phase transition processes and changes related to the thermal properties during heating and cooling of PCMs must be carried out by taking into account the mass ratios of PCM composing materials and applying appropriate methods of characterization. Thus, the experimental investigation of thermo-physical properties of pure and nano- Al₂O₃ added paraffin waxes (PW) in the current study were carried out applying appropriate methods and facilities. Based on the DSC measurements, the latent heats of melting and cooling, phase transition temperature range and specific heat capacity of PCMs were evaluated. The thermal diffusivity of these PCMs as a function of temperature were measured by means of LFA. The density of PCMs were evaluated using density meter.

Majority results of the PCM thermal characterization are provided in Table 1. Latent heats associated with melting and solidification of PW1 were nearly same, around 158 kJ/kg, although, the peaks were 48.31°C (melting) and 41.12°C (solidification) respectively. The phase transition temperature range of PW1 was around 41-55 °C. When nano-Al₂O₃ with the mass fraction of 2% were mixed with PW1, the latent heats of melting and solidification were decreased to 152.98 kJ/kg and 153.07 kJ/kg accordingly. Moreover, the phase transition peaks were slightly shifted to 47.08 °C in and to 41.03 °C respectively.

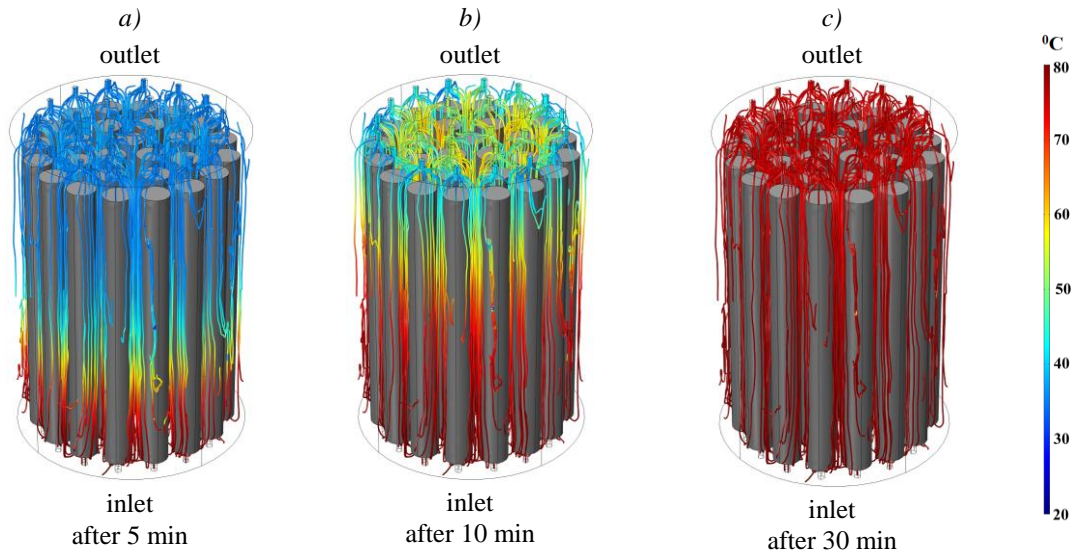


Figure 4. Streamlines of the flow field in the storage tank during charging time

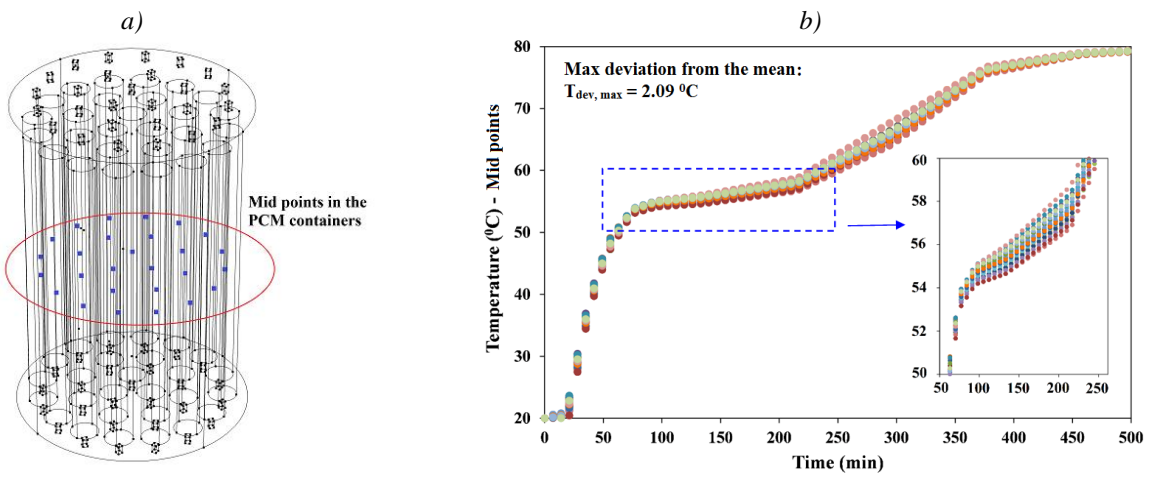


Figure 5. a) Midpoints within PCM containers; b) Temperature evolutions at the midpoints of the PCM containers.

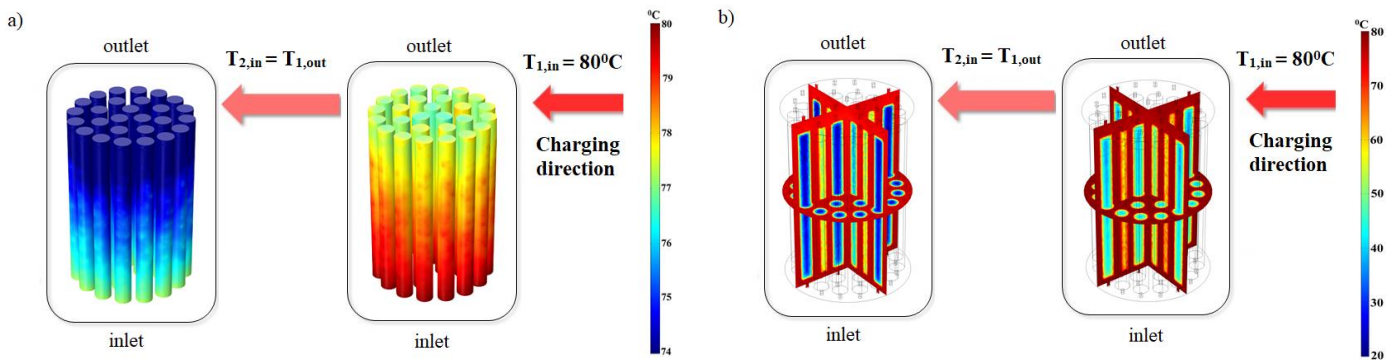


Figure 6. Temperature over the surface of the PCM containers at 40 min charging time with the HTF flow rate of 0.1 m/s at the inlet.

Furthermore, when the mass fraction of nano- Al_2O_3 in the PCM sample were increased up to 4%, the latent heats of melting and solidification continued to decrease and obtained the values of 148.33 kJ/kg and 148.23 kJ/kg respectively, and the phase transition peaks were further shifted down to 46.92 °C and 40.64 °C.

Furthermore, the DSC studies showed that the latent heats of pure PW2 were nearly equal to the value of 183 kJ/kg which are higher than the latent heats of PW1. Phase transition peaks related to melting and solidification of PW2 were 66.29 °C and 59.78 °C respectively. Therefore, PW2 is considered as PCM with high phase change temperature (PCT). Moreover, the studies indicated that PW2 has wider phase transition temperature range, around 52-70 °C compared to PW1. Similar to PW1, mixing of nano- Al_2O_3 with PW2 also resulted in moderate decrease of latent heats and shifts in phase transition peaks as shown in **Ошибка! Неверная ссылка закладки..**

The experimentally measured values of latent heats, phase transition peaks, specific heat capacities, thermal diffusivities and density changes in relation with paraffin waxes, PW1 and PW2, were applied in equations (1.4)-(1.9) in order to numerically study the charging and discharging performance of sequentially connected thermal energy storages, and underhand how nano- Al_2O_3 could influence on their performance.

1.5 Numerical modeling. Validation of the LHS design.

The storage tank was designed in a way that every PCM container in the tank could function as a stand-alone thermal energy storage. Therefore, the number of inlet and outlet tubes arranged at the bottom and on the top of the storage tank were made equal to the number of the PCM containers in order to establish uniform flow distribution around them. To validate the design of TES, the numerical simulation results regarding TES filled with pure PW1 was considered. Thus, the streamlines of the flow field related to the heat transfer fluid in the tank were illustrated in Figure 4 for various charging times, until the heat transfer in the storage tank achieved the steady-state condition. It can be seen that the flow passes the PCM containers uniformly and delivers the thermal energy into the storage tank in a steady manner. Further validation of the design was carried out by studying the temperature evolutions within the PCM containers. Temperature changes as a function of charging time were compared at the midpoints of the PCM containers (midpoint - the central point respect to the height and diameter of the container) and the results were illustrated in Figure 5 for every 10 min of the charging time. According to the data analysis regarding the midpoints, the maximum deviation from the mean temperature change was about 2.09 °C, which means all the PCM containers could be uniformly charged or discharged and each container may function as stand-alone thermal energy storage without significant thermal interaction with the surrounding containers.

The proposed numerical model was further applied to study the energy performance of the sequentially integrated TES and

estimate the effects of nano- Al_2O_3 added paraffin waxes (PW) on the charging processes and efficiencies.

II. SEASONAL ENERGY STORAGE

2.1 Experimental study

Thermal Response Test (TRT) allows to define whether the soil/rock of the terrain is suitable for heat storage, and give essential information about location's geological formation and geophysical properties. The thermal properties like thermal conductivity and thermal resistance can be evaluated accurately using this in-situ method, which is based on analytical Line Source Model (LSM) (Eq. 2.1) [24]:

$$T_{cf,f}(t) = k \cdot \ln(t) + m \quad (2.1)$$

where

$$\lambda = \frac{\dot{Q}}{H \cdot 4\pi \cdot k} \quad (2.2)$$

$$R_b = \frac{H}{\dot{Q}} \left[m - T_g - \frac{\dot{Q}}{H \cdot 4\pi \cdot \lambda} \left(\ln\left(\frac{4\alpha}{r_b^2}\right) - \gamma \right) \right] \quad (2.3)$$

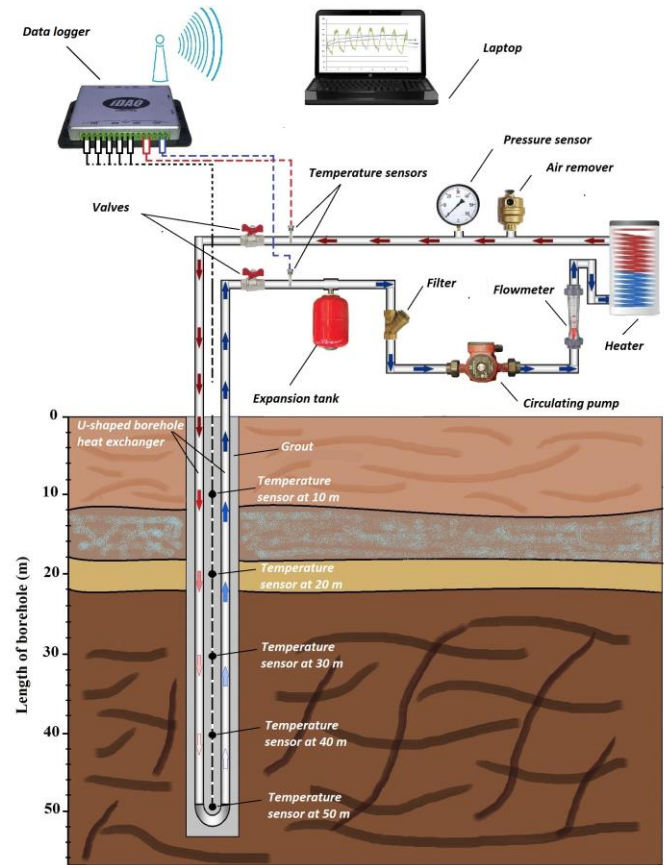


Figure 7. Schematic diagram of the TRT installation and underground layers.

The Line Source Model makes next assumptions: the medium assumed to be homogeneous, the groundwater flows are not considered, and the heat injection is constant during the experiment. The abovementioned assumptions lead to the errors that do not exceed 5%. The TRT installation is schematically illustrated in Figure 7. It consists of equipment such as circulation pump, water heater, expansion tank, pressure sensor, air remover, valves, temperature sensors and connecting pipes. A couple of temperature sensors was mounted to measure inlet and outlet temperatures of BHE and the third one was mounted for measuring the environment temperature. Additional five temperature sensors located at every 10m along the borehole filled with cement and bentonite (grout), the length of borehole frame is 50m. All eight temperature sensors are joined to the data logger, which collects and records the temperature data every one minute throughout the test.

2.2 Geological and hydrogeological structures

Geological and hydrogeological structures of the place were examined during the drilling process of the borehole. Information about the obtained formation layers is given in Table 2. According to the results from 12 to 18 m down the earth the coarse sand layer is detected, and an aquifer was found in this layer. The coarse sand layer is followed by impermeable clay layer with thickness of 4 m. The fine-grained clayey sand which is found from 22-55 m has a water saturation of 10%.

Table 2. Detailed information of rock layers around the borehole

Rock type	Depth (meters)	Thermal conductivity (W/m K)	Volumetric heat capacity (MJ/kg K)	Porosity (%)	Hydraulic permeability (m/s)
Loam	0-12	1.8	3.32	40	$1.16 \cdot 10^{-7}$
Coarse sand	12-18	0.83	3.38	33	$1.16 \cdot 10^{-5}$
Clay	18-22	2.33	1.38	45	$1.16 \cdot 10^{-8}$
Fine-grained clayey sand	22-55	1.75	3.19	35	$1.16 \cdot 10^{-6}$

2.3 Numerical studies and governing equations

Numerical study was conducted for investigating the thermal energy storage in BTES accumulator, with detailed estimation of thermal interaction between BHE and subsurface layers, and for BTES system's construction optimization.

The porosity of the location under consideration has a value ranging from 33 to 45%. The aquifer represents a coarse sand layer with pores saturated with water, therefore in such systems, heat transfers by both conductive and convective ways. Presence of active aquifer is undesirable for BTES construction. In case of high groundwater flow velocity, the convective heat transfer causes large heat losses. Whereas in case of low current velocity the convective heat transfer becomes negligible and the stored heat is not washed away by the water flow. Although if

the current velocity is of order 10^{-9} , then volumetric heat capacity of the layer is doubled which facilitates to achieve a maximum efficiency of BTES accumulator. Therefore, considering of groundwater flow in a mathematical model is very important.

Heat equations. The convective term is added to the traditional nonstationary heat conduction equation in order to take into account the influence of groundwater flow. Thus, heat transfer process in a porous medium are described by the following equation:

$$\begin{aligned}
 (\rho c_p)_{eff} \frac{\partial T}{\partial t} + (\rho c_p)_w \left(u \frac{\partial T}{\partial x} + v \frac{\partial T}{\partial y} + w \frac{\partial T}{\partial z} \right) = \\
 = \frac{\partial}{\partial x} \left((\lambda)_{eff} \frac{\partial T}{\partial x} \right) + \frac{\partial}{\partial y} \left((\lambda)_{eff} \frac{\partial T}{\partial y} \right) + \\
 + \frac{\partial}{\partial z} \left((\lambda)_{eff} \frac{\partial T}{\partial z} \right) + H
 \end{aligned} \quad (2.4)$$

where T - temperature of the porous medium, H - heat source.

At a low velocity of groundwater flow, temperature of soil and fluid is in a local thermal equilibrium and heat transfer in both phases occurs simultaneously. In this case an effective thermal conductivity λ_{eff} (W/mK) and the volumetric heat capacity $(\rho c_p)_{eff}$ ($J/m^3 K$) of the medium are expressed as:

$$\lambda_{eff} = (1 - \phi)\lambda_s + \phi\lambda_w \quad (2.5)$$

$$(\rho c_p)_{eff} = (1 - \phi)(\rho c_p)_s + \phi(\rho c_p)_w \quad (2.6)$$

where ϕ - porosity of the medium, λ_s and λ_w - thermal conductivity and $(\rho c_p)_s$ and $(\rho c_p)_w$ - volumetric heat capacity of the soil and water, respectively.

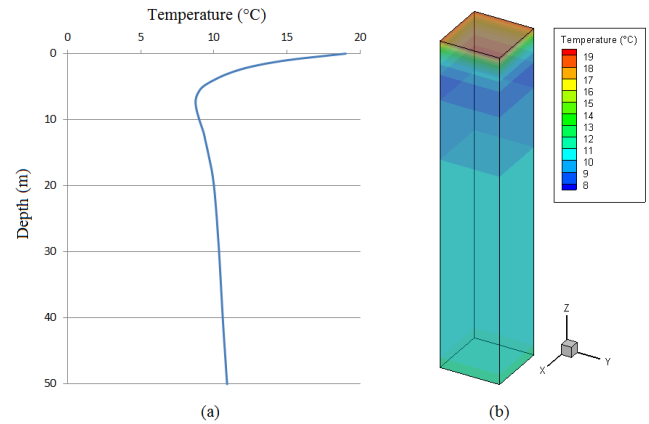


Figure 8. (a) Initial temperature distribution along the borehole, (b) the 3D temperature field.

Initial conditions. Temperature-depth data pairs obtained from TRT test exported to the numerical simulation model as an initial temperature distribution. Temperature data that was obtained for every 10 m were linearly interpolated and the result of interpolation is illustrated in Figure 8.

Boundary conditions. Neumann boundary condition is set, where the upper boundary thermally interacts with air and BHE. Taking into account an constant geothermal heat flux affecting the bottom boundary of BTES, Dirichlet boundary condition is set. The type of conditions that are imposed on the side boundaries depend on the role of the convective and diffusion term in Eq. 16. Aforementioned boundary conditions are described by next mathematical expressions [25], [27-28]:

$$(\lambda)_{eff} \frac{\partial T}{\partial x} n_x + (\lambda)_{eff} \frac{\partial T}{\partial y} n_y + (\lambda)_{eff} \frac{\partial T}{\partial z} n_z = h_{as} (T - T_a) \quad (2.7)$$

$$(\lambda)_{eff} \frac{\partial T}{\partial x} n_x + (\lambda)_{eff} \frac{\partial T}{\partial y} n_y + (\lambda)_{eff} \frac{\partial T}{\partial z} n_z = q_{geo} \quad (2.8)$$

$$(\lambda)_{eff} \frac{\partial T}{\partial x} n_x + (\lambda)_{eff} \frac{\partial T}{\partial y} n_y + (\lambda)_{eff} \frac{\partial T}{\partial z} n_z = 0 \quad (2.9)$$

$$(\lambda)_{eff} \frac{\partial T}{\partial z} n_z = b_{sg} (T - T_g) \quad (2.10)$$

where h_{as} - convective heat transfer of air, q_{geo} - geothermal heat flux, b_{sg} - thermal resistance coefficient between grout and soil, T_a and T_g are temperatures of ambient and grout, respectively.

Momentum equation. The continuity equation describing the mass flow in a unit volume of anisotropic porous medium is [26]:

$$\frac{\partial}{\partial x} \left(k_x \frac{\partial h}{\partial x} \right) + \frac{\partial}{\partial y} \left(k_y \frac{\partial h}{\partial y} \right) + \frac{\partial}{\partial z} \left(k_z \frac{\partial h}{\partial z} \right) + f = 0 \quad (2.11)$$

where h is piezometric head, f is source or sink and k_x, k_y, k_z are hydraulic conductivity in x, y and z directions, respectively.

Initial condition. The initial condition for groundwater at time $t = 0$ is given in the next form:

$$h(x, y, z, t = 0) = h_0(x, y, z) \quad (2.12)$$

Boundary conditions. Groundwater flow occurs on x -direction due to the difference of piezometric heads (Figure 10).

Neumann boundary condition is set on other boundaries, where boundaries are considered as impermeable and groundwater flow is negligible in perpendicular directions to the x -axis.

$$h(x = 0, y, z, t) = h_1 \quad (2.13)$$

$$h(x = l, y, z, t) = h_2 \quad (2.14)$$

$$k_x \frac{\partial h}{\partial x} n_x + k_y \frac{\partial h}{\partial y} n_y + k_z \frac{\partial h}{\partial z} n_z = 0 \quad (2.15)$$

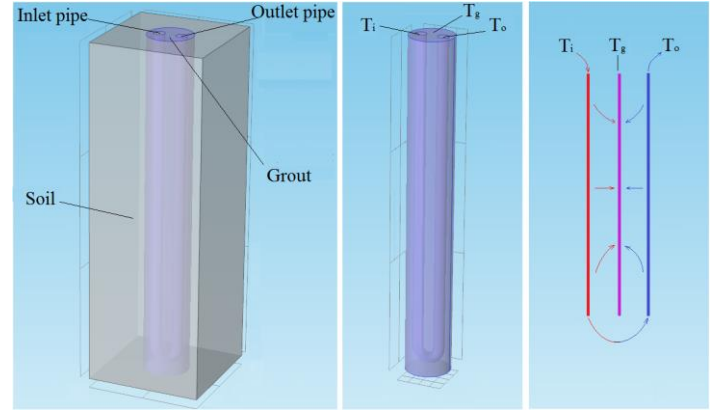


Figure 9. Schematic representation of U-shaped heat pipe.

2.4 Heat transfer in borehole heat exchanger

A single U-shaped BHE consists of inlet and outlet heat pipes, which connected with the U-shaped fitting. It is inserted in the drilled well, which depth constitute 50 m and filled with grout. The diameters of borehole and heat pipes are 160 and 32 mm, respectively. Representation of the area under consideration is shown in Figure 9. The length of BHE is too large in comparison with its diameter and it leads to a numerical problem in grid building. 3D simulation of heat transfers between BHE and the soil require too large number of nodes and realization of such computing volume is not feasible in practice or unavailable and expensive. Therefore, the simulation of the process was implemented in 2 steps: firstly, the amount of specific heat that passes through the unit exterior surface of the grout was calculated; secondly, the obtained specific heat was exported as a heat source to the soil for calculating temperature distribution around the BHE.

Taking into account all aforesaid heat exchange procedure, convective-conductive heat flux between borehole heat exchanger components can be expressed as:

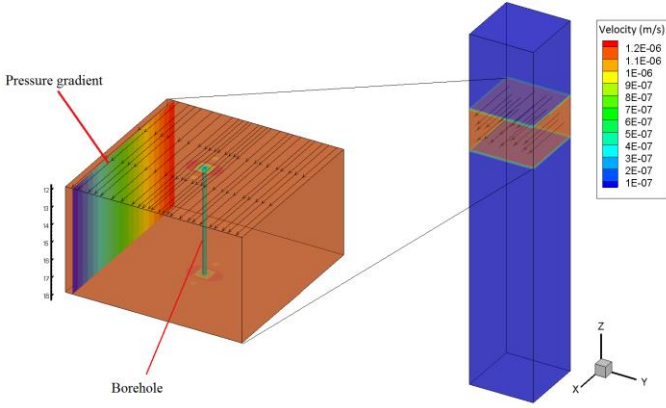


Figure 10. Underground flow

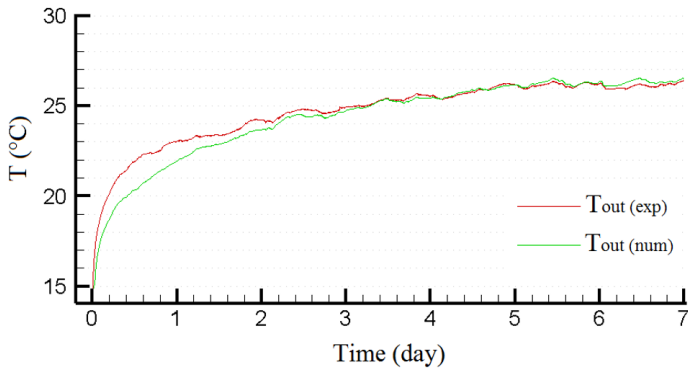


Figure 11. Comparison of experimental and numerical results of temperature values at the BHE outlet.

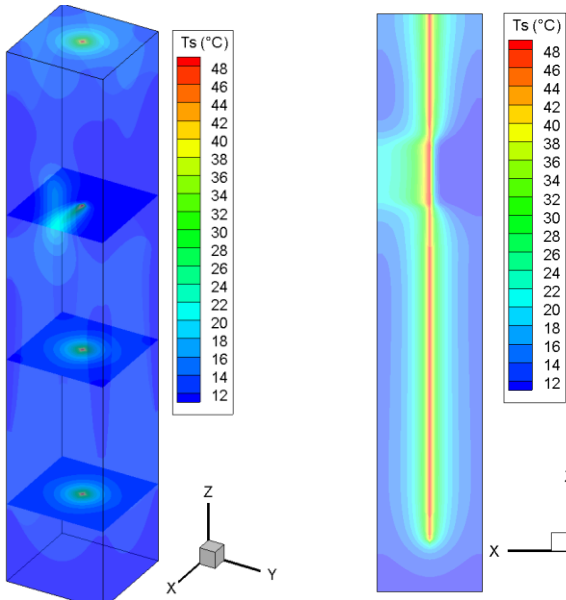


Figure 12. Temperature field prediction for 6 months of charging the BTES.

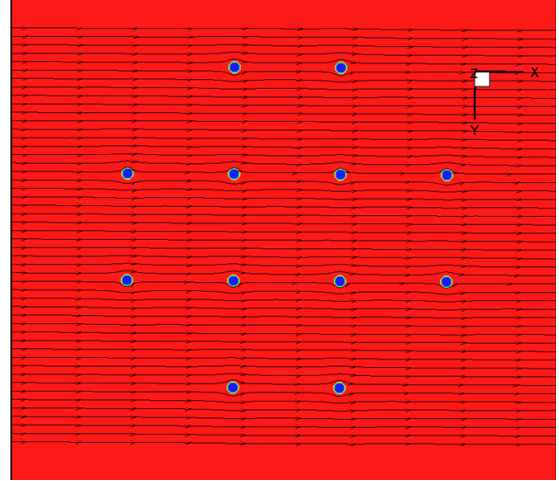


Figure 13. Well pattern of BHE.

$$\begin{aligned} \rho c_{p_w} \frac{\partial T_i}{\partial t} + \rho c_{p_i} w \frac{\partial T_i}{\partial z} &= \\ &= \frac{\partial}{\partial z} \left(\lambda_w \frac{\partial T_i}{\partial z} \right) - \frac{\pi D_{in} b_{ig}}{A_p} (T_i - T_g) \end{aligned} \quad (2.16)$$

$$\begin{aligned} \rho c_{p_o} \frac{\partial T_o}{\partial t} - \rho c_{p_o} w \frac{\partial T_o}{\partial z} &= \\ &= \frac{\partial}{\partial z} \left(\lambda_w \frac{\partial T_o}{\partial z} \right) - \frac{\pi D_{in} b_{og}}{A_p} (T_o - T_g) \end{aligned} \quad (2.17)$$

$$\begin{aligned} \rho c_{p_g} \frac{\partial T_g}{\partial t} &= \frac{\partial}{\partial z} \left(\lambda_g \frac{\partial T_g}{\partial z} \right) + \frac{\pi D_{in} b_{ig}}{A_p} (T_i - T_g) + \\ &+ \frac{\pi D_{in} b_{og}}{A_p} (T_o - T_g) - \frac{\pi D_{in} b_{sg}}{A_p} (T_g - T_s) \end{aligned} \quad (2.18)$$

where T_g and T_i, T_o - the temperature distributions of grout and water in the inlet, outlet heat pipes, respectively, b_{ig} , b_{og} and b_{sg} are coefficients characterizing the thermal resistance of materials, D_{in} is the outer diameter and is the cross-sectional area of pipes.

Figure 11 shows a good agreement of numerical results with experimental data with the deviation of 3.3%. An improved mathematical model very well describes heat transfer processes in BTES. This mathematical model will be used for further numerical studies. Temperature distribution on the vicinity of heat exchanger is shown in Figure 12 for 6 months of charging the geothermal accumulator, when the rate of the underground flow was 10 cm per day.

In Figure 13 the well pattern consisting 12 BHE illustrated.

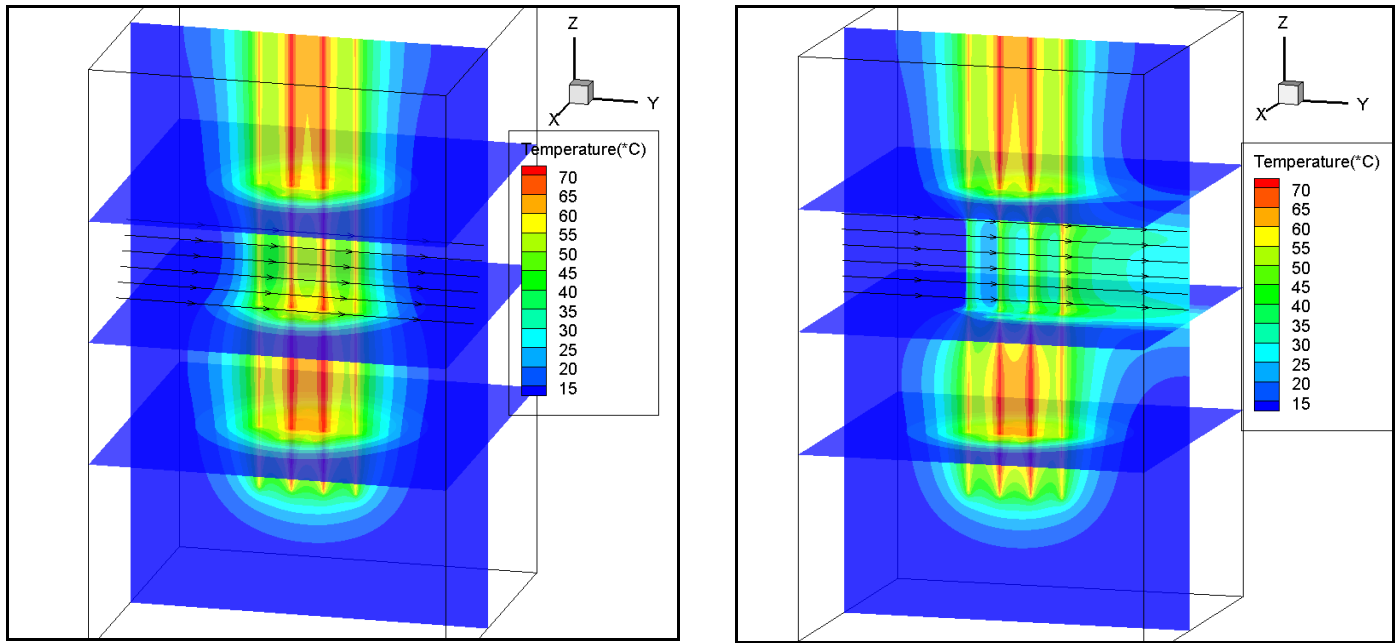


Figure 14. Array of 12 BHE for large scale energy storage systems: a) for the case of inactive aquifer, b) for the case of active aquifer.

CONCLUSION

In the present paper the performance of Hybrid Thermal Energy Storage system analyzed: at first the performance of the STS accumulator was numerically investigated for two PCM materials with different phase change temperatures. The mathematical model allows to define the effective working fluid injection rates and to calculate the amount of energy needed for fully charging the STS accumulator.

Well logging and in-situ TRT test results gave essential information about the soil structure and place's applicability for heat storage purposes. Experimental results revealed the presence of an aquifer from 12 to 18 m, therefore the mathematical model constructed for describing heat transfer processes considers the convective heat transfer caused by underground water flows. Complex geometry of the calculation domain was implemented in two steps. U-shaped BHE and the grout that was used to fill the space between borehole walls and heat exchanger was simulated 3D, and the amount of heat that passes through the outer surface was recorded and used in calculating the temperature field in the geothermal accumulator. When simulating the heat transfer in the BTES accumulator the heat that comes from BHE was implemented as a linear source, because the height of the wells is very big compared to well diameter.

The present paper shows temperature distribution in the geothermal accumulator for the cases of active and inactive aquifers. The verification of the numerical results with experimental data from the TRT studies, which carried out at the Agro-Bio Center of KazNU, shows a good agreement.

ACKNOWLEDGMENTS

This research is supported by Grant № APP-JRG-16/0071P, awarded by The Science Committee of the Ministry of Education and Science of the Republic of Kazakhstan within the "Fostering Productive Innovation" Project.

REFERENCES

1. Boeck L, Verbeke S, Audenaert A, Mesmaeker L. Improving the energy performance of residential buildings: A literature review. *Ren Sus Eng Rev* 2015;52:960-75
2. Fabrizio E, Seguro F, Filippi M, Integrated HVAC and DHW production systems for Zero Energy Buildings. *Ren Sus Eng Rev* 2014, 40: 515-541.
3. Xu B, Li P, Chan C. Application of phase change materials for thermal energy storage in concentrated solar thermal power plants: A review to recent developments. *Appl Energy* 2015;160:286-307
4. Cunha J, Eames P, Thermal energy storage for low and medium temperature applications using phase change materials – A review. *Appl Energy* 2016;177:227-238
5. M. Khodadadi, L. Fan, and H. Babaei, "Thermal conductivity enhancement of nanostructure-based colloidal suspensions utilized as phase change materials for thermal energy storage: A Bibliography review," *Renew. Sustain. Energy Rev.*, vol. 24, pp. 418–444, 2013
6. J. M. Mahdi and E. C. Nsofor, "Solidification of a PCM with nanoparticles in triplex-tube thermal energy storage system," *Appl. Therm. Eng.*, vol. 108, pp. 596–604, 2016
7. Khan Za, Khan Zu, Ghafoor A. A review of performance enhancement of PCM based latent heat storage system

- within the context of materials, thermal stability and compatibility *Energy Convers Manage* 2016; 115:132-58
8. Pielichowska K, Pielichowski K. Phase change materials for thermal energy storage. *Progr Mater Sci* 2014;65:67-123
 9. Sharma R, Ganesan P, Tyagi V, Metselaar H, Sandaran S. Developments in organic solid–liquid phase change materials and their applications in thermal energy storage, *Energy Conve Manage* 2015; 95:193-228
 10. Rathod M, Jyotirmay B. Thermal stability of phase change materials used in latent heat energy storage systems: A review. *Ren Sus Eng Rev* 2013;18:246-58
 11. Shaikh S, Lafdi K, Hallinan K. Carbon Nanoadditives to Enhance Latent Energy Storage of Phase Change Materials, *Jour Appl Phys* 2008;103: 094302:1-6
 12. Xu B, Li Z, Paraffin/diatomite/multi-wall carbon nanotubes composite phase change material tailor-made for thermal energy storage cement-based composites. *Energy* 2014; 72:371-80
 13. Li M, A nano-graphite/paraffin phase change material with high thermal conductivity. *Appl Energy* 2013;106:25:30
 14. Li Y, Li J, Guan W, Wang X, Qian T. Preparation of paraffin/porous TiO₂ foams with enhanced thermal conductivity as PCM, by covering the TiO₂ surface with a carbon layer. *Appl Energy* 2016; 171:37-45
 15. Xiao X, Zhang P, Li M. Preparation and thermal characterization of paraffin/metal foam composite phase change material. *Appl Energy* 2013;11:1357-66
 16. Wang C, Lin T, Zheng H. Heat transfer enhancement of phase change composite material: Copper foam/paraffin. *Renew Energy* 2016;96:960-65
 17. Li WQ, Qu ZG, He YL, Tao WQ. Experimental and numerical studies on melting phase change heat transfer in open-cell metallic foams filled with paraffin. *Appl Therm Eng* 2012;37:1-9
 18. Lin S, Al-Kayiem H, Evaluation of copper nanoparticles – Paraffin wax compositions for solar thermal energy storage. *Solar Energy* 2016;132:267-278
 19. Elfasakhany A, Performance assessment and productivity of a simple-type solar still integrated with nanocomposite energy storage system, *Applied Energy* 2016; 183:399-407
 20. Chen C, Zhang H, Gao X, Xu T, Fang Y, Zhang Z, Numerical and experimental investigation on latent thermal energy storage system with spiral coil tube and paraffin/expanded graphite composite PCM, *Energy conversion and management* 2016; 126:889-897
 21. Al-abidi A, Mat S, Sopian K, Sulaiman M.Y, Mohammed A, CFD applications for latent heat thermal energy storage: a review. *Renewable and Sustainable Energy Reviews* 2013;20:353-363
 22. Niyas H, Prasad S, Muthukumar P, Performance investigation of a lab–scale latent heat storage prototype - Numerical results. *Energy Conversion and Management*, 2017;135:188-199
 23. Youssef W, Ge Y, Tassou S.A., CFD modelling development and experimental validation of a phase change material (PCM) heat exchanger with spiral-wired tubes. *Energy Conversion and Management* 2018;157:498-510
 24. W. Choi, R. Ooka, Effect of disturbance on thermal response test, part 1: Development of disturbance analytical model, parametric study and sensitivity analysis, *Renewable Energy* 85(2016) 306-318.
 25. W. Jürges, Der warmeübergang an einer ebenen wand (heat transfer at a plane wall, *Gesundheits-Ingenieur (Beihefte 1)* (1924).
 26. W.H. McAdams, *Heat Transmission*, third ed., McGraw-Hill, New York, 1958.
 27. Al-Khoury R., Bonnier P. G. and Brinkgreve R. B. J., Efficient finite element formulation for geothermal heating systems // *International journal for numerical methods in engineering*.-2005. -P. 988-1013.
 28. Al-Khoury R., Nabi M., An efficient finite volume model for shallow geothermal systems. Part I:Model formulation // *Computers & Geosciences*.-2012. –Vol.49, -P. 290-296